Journal of Materials Research and Technology 35 (2025) 6397–6407

Contents lists available at ScienceDirect

Journal of Materials Research and Technology

journal homepage: www.elsevier.com/locate/jmrt

Quantifying chemical homogeneity across the melt pool in laser powder-bed fusion of metallic glass matrix composites from blended elemental powders

P. Wannapraphai [a], C. Panwisawas [b], O.S. Houghton [c], J. Shinjo [d], H. Wakabayashi [d], T. Phetrattanarangsi [a], S. Kuimalee [e], R.C. Reed [f], A.L. Greer [c], B. Lohwongwatana [a], C. Puncreobutr [a,*]

[a] Department of Metallurgical Engineering, Faculty of Engineering, Chulalongkorn University, Bangkok, 10330, Thailand
[b] School of Engineering and Materials Science, Queen Mary University of London, London, E1 4NS, United Kingdom
[c] Department of Materials Science and Metallurgy, University of Cambridge, Cambridge, CB3 0FS, United Kingdom
[d] Next Generation Tatara Co-Creation Centre (NEXTA), Shimane University, 1060, Nishikawatsu, Matsue, 690-8504, Japan
[e] Industrial Chemistry Innovation Programme, Faculty of Science, Maejo University, Chiang Mai, 50290, Thailand
[f] Department of Materials, University of Oxford, Parks Road, Oxford, OX1 3PH, United Kingdom

ARTICLE INFO

Handling Editor: P Rios

Keywords:
Metallic-glass-matrix composite
Laser powder-bed fusion
Ti-based alloys
Melt-pool dynamics
Heterogeneity

ABSTRACT

Additive manufacturing (AM) with blended elemental powders offers an opportunity to reduce processing time and cost whilst increasing the range of alloys that AM can produce — it is possible to print alloys that are difficult to produce from pre-alloyed powders. Metallic-glass-matrix composites (MGMCs) are an example of such alloys. Their microstructures are complex, and printing parameters must balance the rapid cooling required for glass formation with achieving appropriate microstructural control to deliver favourable mechanical properties. Their uncommon compositions also mean that sourcing alloyed powder is challenging. Blended powder mixtures with overall composition $Ti_{58.5}Zr_{31.5}Cu_{10}$ (at.%) were processed using laser powder-bed fusion (L-PBF) to produce a β-(Ti, Zr) phase reinforced MGMC. The influence of volumetric energy density (VED) on powder mixing was investigated by experimental study and thermal fluid-flow simulations based on computational fluid dynamics. At low VED, a lack of complete melting and mixing in each melt pool is seen due to a lack of convective flow. To interpret this chemical inhomogeneity, a graphical method for interpreting heterogeneity is introduced, offering a broader application for AM processes utilising blended powders. The implications of requiring higher VED to enhance chemical homogeneity in blended powders are discussed, particularly concerning the production of metallic glasses and MGMCs via AM.

1. Introduction

Metallic glasses (MGs) and metallic glass matrix composites (MGMCs) have attracted substantial interest from multiple fields due to their unique array of mechanical properties [1–6]. MGMCs with low elastic modulus are attractive for biomedical implants in load-bearing applications to reduce the risk of stress shielding, implant loosening, and bone resorption [7,8]. Some MGs have also demonstrated superior corrosion resistance compared to their crystalline counterparts in simulated body fluids [9–11], and compositions that are functionalised with antibacterial properties are of potential interest for the next generation of implants [12,13].

Despite a range of attractive properties for biomedical applications, the use of MGs remains limited. Any alloy development strategy must possess the critical target properties for a specific application and a broad range of other properties. Since MGs must be formed at high cooling rates to avoid crystallisation, there are a limited number of known compositions with sufficient glass-forming ability (GFA) to produce components for biomedical applications [14,15]. MGs also lack plasticity in tension (deformation occurs via the catastrophic propagation of shear bands). This often leads to a low fracture toughness; those MGs with high fracture toughness are typically formed from 'fragile'

* Corresponding author.
E-mail address: chedtha.p@chula.ac.th (C. Puncreobutr).

https://doi.org/10.1016/j.jmrt.2025.02.204
Received 16 December 2024; Received in revised form 7 February 2025; Accepted 22 February 2025
Available online 22 February 2025

liquids [16], which have insufficient GFA to be cast fully amorphous in thick sections. In contrast, MGMCs (where a mechanically ductile crystalline phase co-exists with an amorphous phase) can possess much higher strength, higher fracture toughness, and adjustable elastic modulus [17–19].

Additive manufacturing (AM) has recently gained attraction as a useful processing technique for MGs and MGMCs [6,20–25]. Since glass formation occurs in each melt pool, the requirement of high cooling rates to form a glass is decoupled from the size of the component being produced. Though MGs can be processed by thermoplastic forming (TPF), the process is limited to simple geometries, requires costly equipment not typically used to process metals and is particularly challenging for MGMCs. In most industrial scenarios, AM components are processed from pre-alloyed powders. Alloying powders to achieve the same composition as the printed part is typical for studies of processing Fe-, Zr- and Ti-based MGs by laser powder-bed fusion (L-PBF) [26,27]. This additional pre-alloying step is costly and time-consuming, limits the degree of freedom in alloy design and reduces flexibility in supply chains. Blended elemental powders are a potential feedstock for low-cost and time-efficient processing of MGs and MGMCs in laboratory and commercial environments.

Ti–Zr–Cu MGMCs, where β-(Ti, Zr) dendrites co-exist with a Cu-rich amorphous matrix, have been produced from elemental powders with attractive mechanical properties [28–30]. The excellent biocompatibility of Ti and Zr makes these MGMCs a prospective material for biomedical implants. In having only three elements, this system is also simpler to model and understand than other MGMCs; it is an ideal candidate to understand the processing of MGMCs by AM.

Volumetric energy density (VED) is widely used in L-PBF process to optimise melt pool stability and microstructural evolution. However, its predictive capability is limited as it does not account for Marangoni-driven convection, keyhole instability, or localized thermal gradients [31]. Convective melt pool flow significantly influences chemical homogeneity, but VED-based models do not capture these effects [32]. Additionally, variations in melt pool hydrodynamics contribute to porosity formation and solute redistribution, further demonstrating VED's limitations [33]. The interaction between thermal gradients, fluid flow, and vaporisation also impacts microstructural evolution, affecting alloy performance [34]. Studies show that keyhole oscillations, spatter formation, and laser absorption efficiency further complicate the predictability of melt pool dynamics [35,36]. Overcoming these limitations is crucial for achieving accurate process control, enhancing alloy homogeneity, and optimising mechanical properties in L-PBF.

The present work studies the chemical and microstructural heterogeneity in samples processed by L-PBF from blended powder of nominal composition $Ti_{58.5}Zr_{31.5}Cu_{10}$ (at.%). Three different sets of processing parameters are studied experimentally and by thermal fluid-flow simulations using computational fluid dynamics (CFD). To analyse the heterogeneity across each melt pool, this study introduces a novel graphical interpretation method for analysing chemical heterogeneity in L-PBF processed Ti–Zr–Cu alloys, utilising ternary chemical heatmaps to visualise mixing efficiency. Additionally, the introduction of the H factor provides a systematic metric for quantifying compositional homogeneity within the melt pool. In combining experimental work with computational modelling by extending beyond conventional VED-based approaches, understanding can be developed beyond a simple refinement of parameters [26,37–40]. The combination of thermal fluid-flow simulations and experimental studies helps to understand the necessary conditions for successful mixing of blended powders and the challenges these conditions present in achieving metallic glasses (MGs) and metallic glass matrix composites (MGMCs) with desirable end properties for the target application.

2. Method

2.1. Sample preparation

Commercially pure elemental powders (>99% wt.%) of titanium (AP&C, Canada), zirconium (Nanoshel, USA), and copper (H.C. Starck, Germany) were used as precursor feedstock. Before mixing, particle size and morphology were characterised using scanning electron microscopy (Thermo-Fischer Quanta 250 FEG) and a particle-size analyser (Mastersizer 3000, Malvern Panalytical, UK). Particles were spherical (Fig. 1a–c), and their sizes lognormally distributed (Fig. 1d). The median particle diameter (D50) for each powder was 29.5 μm (Ti), 31.0 μm (Zr) and 25 μm (Cu).

To blend the elemental powders for printing, Ti, Zr, and Cu were mixed in the correct ratio to achieve the desired alloy composition, $Ti_{58.5}Zr_{31.5}Cu_{10}$ (at.%). This was performed in an inert atmosphere with an electric tumbler (Inversina 2L, Bioengineering AG, Switzerland) for 3 h at 12 RPM. After mixing, the powder was analysed to assess homogeneity (Fig. 1d).

Specimens with dimensions of $5 \times 5 \times 5$ mm^3 were fabricated in a high-purity argon atmosphere with a Concept Laser 200R machine (GE additive, MA). The chamber's oxygen level was regulated to a maximum of 1000 ppm. For all samples, the laser power was set to 95 W with a hatch spacing of 30 μm. A 30 μm layer of powder was deposited for each laser scan, and a chessboard scanning strategy was used to minimise residual stress [41]. The laser scan speed was set to 3000, 1300, and 960 mm s^{-1} to achieve volumetric energy densities (VED) of 35, 80 and 110 J mm^{-3}, respectively. These are subsequently referred to as E35, E80 and E110, respectively.

2.2. Characterisation

X-ray diffraction (XRD) was performed on a Malvern Analytical diffractometer with Cu (λ Kα = 1.54 Å) radiation. Scanning electron microscopy was performed on a Thermo Fischer Quanta 250 FEG in BSE mode with 15 kV accelerating voltage. Microscopic chemical mapping was performed via energy-dispersive X-ray spectroscopy (EDX) with 15 kV accelerating voltage using an electron-probe micro-analyser (EPMA-8050G, Shimadzu, Japan).

Scanning transmission electron microscopy (STEM) was performed on a lamella prepared from a polished section of sample E35. The lamella was cut using gallium ion milling (at 30 kV, 90 pA–1.4 nA) with an FEI NanoLab-600 Helios dual-beam focused ion beam (FIB) microscope, equipped with an Omniprobe-200 micromanipulator. In this case, the cross-sectional lamellae were approximately 5×20 μm^2 in area, thinned to approximately 50 nm at the original sample surface using the gallium ion beam.

STEM investigation was performed on an FEI Tecnai Osiris equipped with a high-brightness FEI XFEG gun, operating at an accelerating voltage of 200 kV. Diffraction patterns were recorded at a camera length of 550 mm with a Gatan UltraScan1000XP with 2048 × 2048 pixels. EDX data collected using an FEI Super-X system with four Bruker Si-drift detectors were analysed with Hyperspy.

Hardness testing of the as-printed samples was conducted using a Vickers hardness tester (Mitutoyo MVK-H2 Microhardness Tester, Japan) with a load of 500 gf and a dwell time of 10 s. A minimum of 50 indents were made on each sample, and the average hardness values were calculated. These results were then correlated with observed microstructural heterogeneities to evaluate the effect of energy density on mechanical properties.

2.3. Computational modelling of in-situ alloying

The equilibrium phase diagram and isothermal sections of Ti–Cu–Zr composition space were assessed via CALPHAD using Thermo-Calc software (Thermo-Calc, Sweden) and its high entropy alloy database,

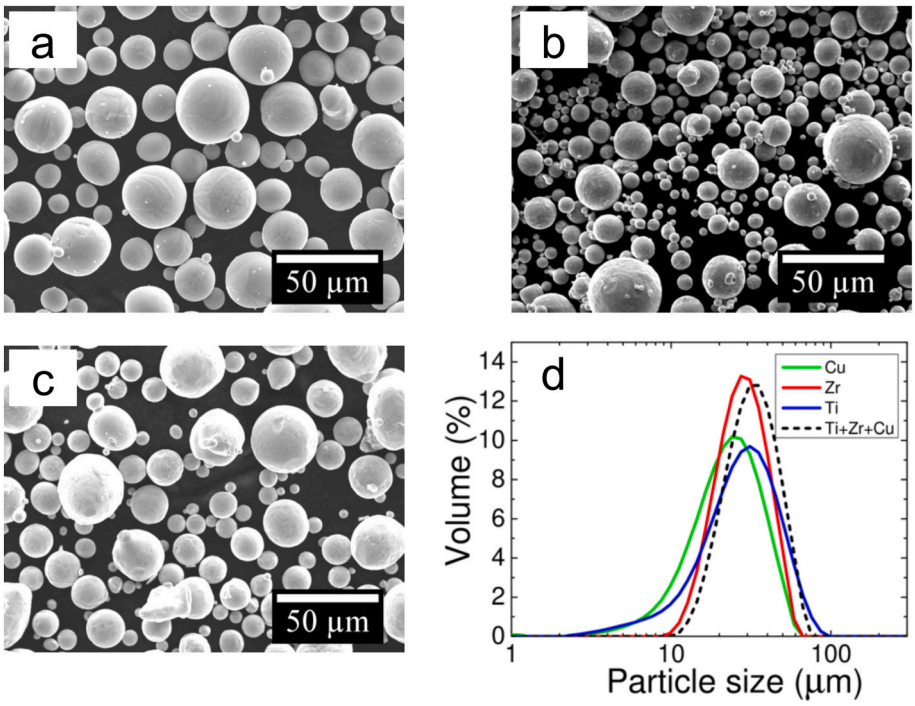

Fig. 1. Secondary-electron micrographs of (a) Ti, (b) Zr, and (c) Cu elemental powders. (d) Particle size distribution of each elemental powder and the blended powder after mixing.

TCHEA4.

Thermal fluid-flow simulation based on computational fluid dynamics (CFD) was performed to complement experimental results. For this particular scenario, the equations of mass, momentum, energy and elements in the non-conservative form are [42,43]:

$$\frac{\partial \rho}{\partial t} + (u \bullet \nabla)\rho = -\rho \nabla \bullet u, \tag{1}$$

$$\frac{\partial u}{\partial t} + (u \bullet \nabla)u = -\frac{\nabla p}{\rho} + Q_{u,i} + g + F_{u,surf}, \tag{2}$$

$$\frac{\partial T}{\partial t} + (u \bullet \nabla)T = -\frac{\rho \nabla \bullet u}{\rho c_p} + Q_T, \tag{3}$$

$$\frac{\partial Y_i}{\partial t} + (u \bullet \nabla)Y_i = \frac{1}{\rho}\nabla \bullet (\rho D \nabla Y_i), \tag{4}$$

where ρ is the density, u is the velocity, T is the temperature, p is the pressure and Y_i is the mass fraction of elements i (Ti, Zr and Cu).

Q_u in Eq. (2) represents the viscous force and Darcy's force in the mushy zone, given by:

$$Q_{u,i} = \frac{1}{\rho}\frac{\partial \tau_{ij}}{\partial x_j} - \frac{v}{K}\left(\frac{(1-f_L)^2}{f_L^3}\right)u_i, \tau_{ij} = u\left(\frac{\partial u_i}{\partial x_i} + \frac{\partial u_j}{\partial x_i}\right) - \frac{2}{3}\mu \nabla \bullet u \delta_{ij} \tag{5}$$

where K is the permeability coefficient and f_L is the liquid fraction, g is the gravitational acceleration, and $F_{u,surf}$ represents the interfacial surface tension force including the Marangoni effect and the recoil pressure.

Q_T in Eq. (3) represents the heat transport including heat conduction by Fourier's law, enthalpy transport by mass diffusion, work done by viscous forces, latent heat of transformation and radiation. This is given in the form:

$$Q_T = \frac{1}{\rho c_p}\left[\nabla \bullet (\lambda \nabla T) - \nabla \bullet \left(\rho \sum h_i Y_i V_i\right) + \frac{\partial \tau_{ij} u_i}{\partial x_j} - \frac{D \sum \rho Y_i \Delta h_i}{Dt}\right] + \varepsilon \sigma_{SB}\left(T^4 - T_0^4\right)|\nabla \phi| \tag{6}$$

where V_i is the diffusion velocity formulated by Fick's law and Δh_i is the latent heat of elements i. Radiation on the heated metal surface is accounted for by the gradient of the interface-identifying colour function $|\nabla \varphi|$, with σ_{SB} the Stefan-Boltzmann constant and ε the emissivity. The laser beam is traced by the ray-tracing method to give heat input to the exposed surface.

The liquid/gas interface is captured by the coupled level-set and volume-of-fluid (CLSVOF) method [42] to assure accuracy of shape and conservation of volume. The level-set function F is a signed distance function where $F = 0$ represents the interface, $F > 0$ the liquid/solid phase and $F < 0$ the gaseous phase. F is evaluated from the equation:

$$\frac{\partial F}{\partial t} + (u \bullet \nabla)F = |\nabla F|\frac{dN}{dt} \tag{7}$$

where dN/dt represents the surface regression speed due to evaporation. The equivalent equation for volume is solved to correct F so that its volume is conserved. By converting F into a Heaviside function φ $(0 \le \varphi \le 1)$, for example, the density is given by $\rho = (1 - \varphi)\rho_G + \varphi\rho_L$; ρ_L and ρ_G are the liquid and gas density, respectively.

The numerical code used in this work is the proprietary code TATM-MEX; a more detailed description can be found in Ref. [42]. The code has been confirmed for various benchmark tests, such as surface tension including the Marangoni effect, heat transfer, vaporisation, liquid/gas phase transformation (boiling) and multi-species mixing [42]. The computational domain size was 590 μm × 280 μm × 470 μm and the grid resolution was 4 μm. This resolution was found to be sufficient to capture the microscopic melt pool fluid flow dynamics. Powders, scaled to be congruent with the experimental size, were deposited onto a Ti substrate with the layer thickness of 30 mm. The molar ratio was set the same as experimental work reported here (X_{Ti}: X_{Zr}: X_{Cu} = 0.585: 0.315: 0.1), and the spatial powder distribution was randomly determined.

Comparisons were made for two values of the energy density, $E = 35$ J mm^{-3} and $E = 80$ J mm^{-3}, to see the effect of the energy density on changing the glass-forming ability in terms of mixing and cooling characteristics.

3. Results

3.1. Characterisation of printed microstructures

X-ray diffraction (XRD) patterns and BSE micrographs of three samples printed with different volumetric energy densities (VEDs) show different microstructures (Fig. 2). At high VED (110 J mm^{-3}), complete melting results in a microstructure of β-(Ti,Zr) surrounded by (Ti,Zr)$_2$Cu (Fig. 2a and b) [28,29,44]. The morphology highlights the geometry of each melt pool; the features suggest solidification progressing radially inwards from the boundary towards the centre of the melt pool, with the microstructure becoming finer due to variation in cooling rate.

As the VED is reduced, the microstructure becomes less homogeneous. XRD patterns and BSE micrographs reveal unmelted Ti and Zr powder in samples E80 (Fig. 2c,d) and E35 (Fig. 2e and f). This is likely due to lack of energy input at lower energy density. A complex microstructure is observed in the E35 sample, consisting of crystalline reflections for unmelted Ti and Zr powder, β-(Ti,Zr) and (Ti,Zr)$_2$Cu superimposed on the broadened peak. The increase in peak broadness corresponds to a finer microstructure for melted regions. Owing to the relative intensity of crystalline reflections to diffuse amorphous halo, the presence of a minority glassy phase is not conclusively shown from XRD patterns for the studied composition [45–48].

Chemical mapping of representative regions for each sample shows that Cu and Ti strongly segregate away from one another (Fig. 3). For E110, the reproducibility of microstructural features across each melt pool is consistent with complete mixing (Fig. 3a–c). Coarse Cu-rich regions decorate the edge of the melt pool, which become finer with the overall microstructural scale towards the centre. In contrast, E80 (Fig. 3d–f) and E35 (Fig. 3g–i) show pronounced chemical inhomogeneity between each melt pool, consistent with the unmelted/enriched regions observed in BSE micrographs. In regions where more mixing occurs, the compositional gradients within the fine microstructure cannot be resolved. Their features appear consistent with the features observed in E110.

Though qualitative trends are convenient, quantitative analysis helps to guide the refinement of processing parameters. For each EPMA pixel (encompassing 500 × 375 pixels), the chemical composition is calculated at each point by normalising the EPMA count relative to references for each pure element. The composition at each pixel across the image can be plotted on a histogram or 'heatmap' in ternary composition space (Fig. 4a–c). This can then be compared to the equilibrium phase diagram and liquidus projections (Fig. 4d) predicted by CALPHAD.

This graphical interpretation enables understanding of both compositional variation and microstructural scale: as the microstructure becomes finer, the 'heatmap' intensity should increase about the nominal composition; increased chemical homogeneity should result in less scatter. In the present work, for low VED (E35), substantial scatter is observed (Fig. 4c), which predominantly corresponds to the presence of unmelted and partially melted regions. As the VED increases, reduced scatter corresponding to more complete melting is observed (Fig. 4b). For E110, the composition distribution is relatively narrow and primarily centred around the nominal alloy composition (Fig. 4a).

The parameter H is introduced to quantify heterogeneity in the system:

$$H = \frac{\sum_{ij}\left(x_{ij} - n_i\right)^2}{\sum_{ij}\left(\Delta_i\right)^2} \tag{8}$$

where j is a particular spatial pixel, i is each element (Cu, Ti and Zr), x is the mole fraction of element i at spatial pixel j, n is the mole fraction of the nominal composition and:

$$\Delta_i = \max(n_i, 1 - n_i). \tag{9}$$

The numerator represents the sum of the squared deviations of the mole fractions of each element, and the denominator represents the sum of the maximum squared deviations for each element across every pixel. The value of H ranges between 0 and 1, where a lower value of H

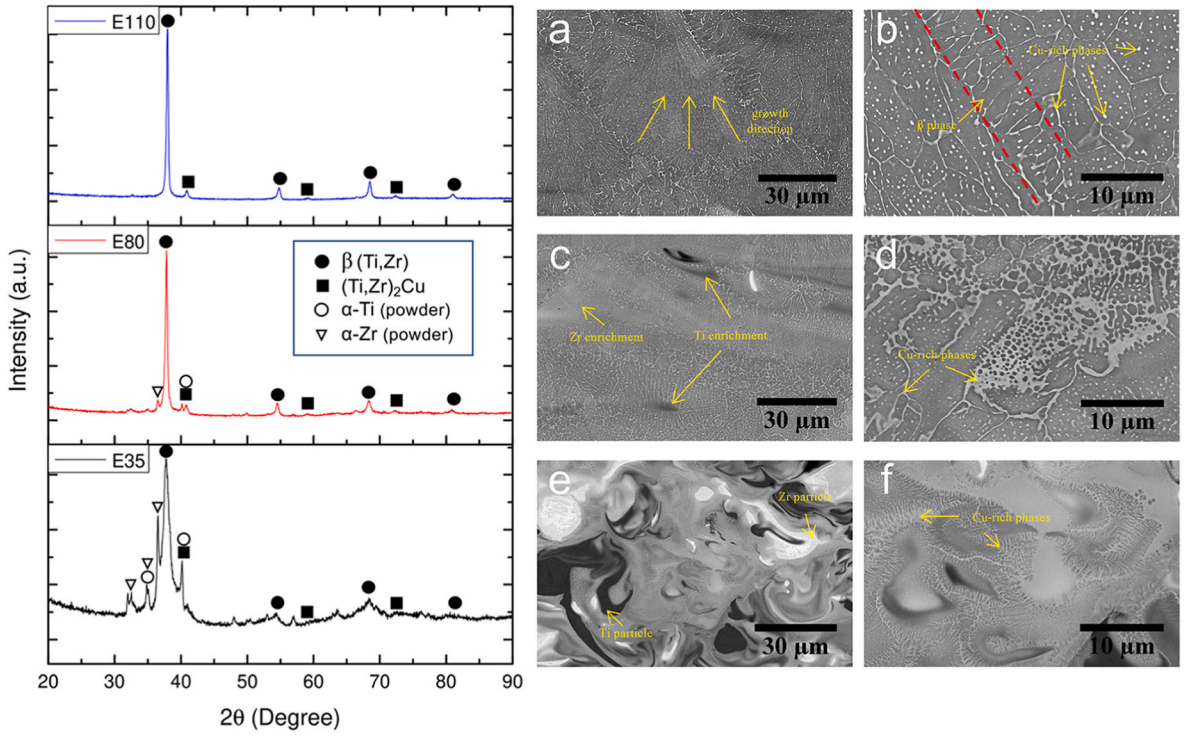

Fig. 2. (left) XRD results for as-printed $Ti_{58.5}Zr_{31.5}Cu_{10}$ (at. %) specimens at energy densities of E = 35 J mm^{-3} (E35), E = 80 J mm^{-3} (E80) and E = 110 J mm^{-3} (E110). Peaks characteristic of each crystalline phases are labelled. Corresponding BSE micrographs are shown in (a,b) for E110, (c,d) for E80 and (e,f) for E35. Dashed red lines indicate the region of a heat affected zone (HAZ) around a melt pool.

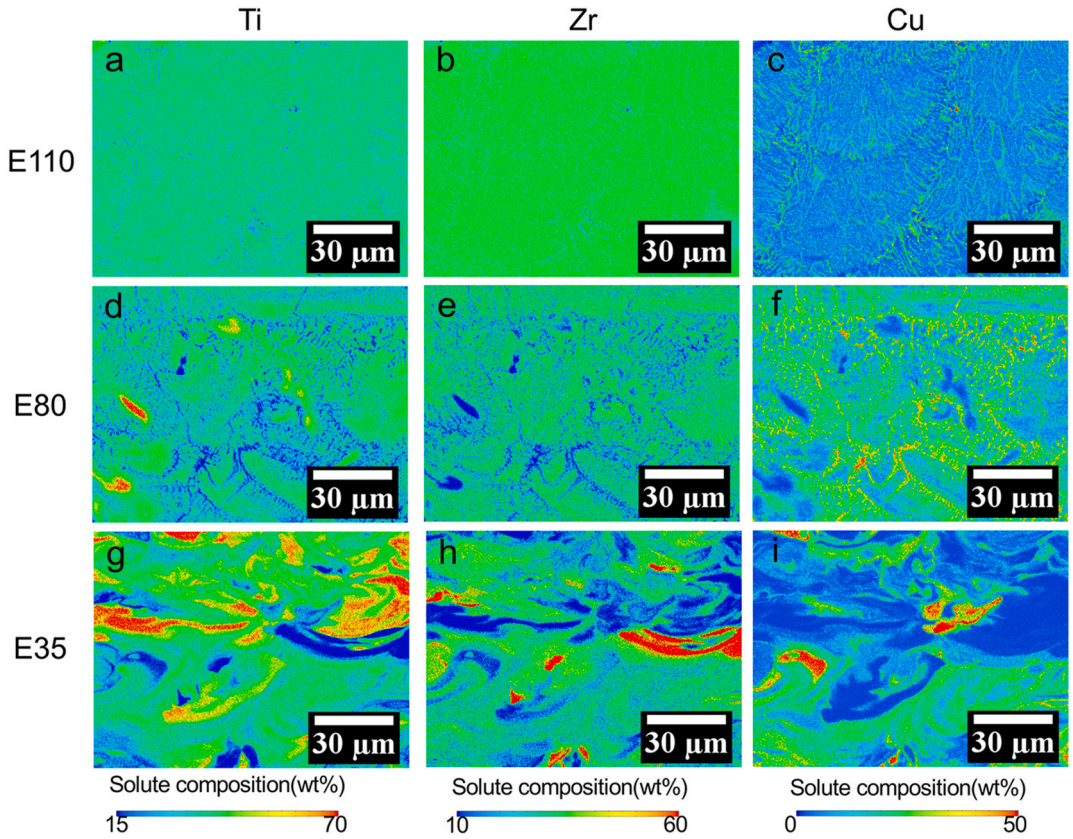

Fig. 3. Chemical maps obtained by EPMA to show the distribution of constituent elements within the specimens fabricated with VEDs of (a–c) 110 J mm^{-3}, (d–f) 80 J mm^{-3}, and (g–i) 35 J mm^{-3}.

indicates improved compositional homogeneity and a fine microstructure.

In this case, *H* cannot be equal to 0 as the microstructure is composed of neither a single phase nor distinct structural phases. The *H* values for each sample were 0.31 (E35), 0.23 (E80), and 0.21 (E110). Consistent with qualitative trends, *H* decreases with increasing VED.

The observed chemical inhomogeneity across different energy densities directly influences mechanical properties. To assess this effect on hardness, Vickers hardness testing was performed, measuring overall specimen hardness rather than individual phases. The results, presented in Table 1, show average hardness values of 380 ± 22 HV (E110), 404 ± 48 HV (E80), and 406 ± 51 HV (E35), which align well with previous studies on similar alloy systems [29]. High-VED specimens exhibit greater consistency, whereas low-to medium-VED specimens show increased variation, likely due to microstructural heterogeneity. For reference, pure Ti and Zr have hardness values of 200–259 HV and 196–221 HV, respectively [49,50]. The presence of unmelted particles negatively impacts hardness, particularly in low-VED specimens, while higher VED promotes uniformity.

To provide confirmation of a glassy phase, an electron-transparent lamella was prepared from sample E35. STEM EDX, shown in Fig. 5a, mapping shows pronounced chemical segregation, consistent with chemical mapping by EPMA and BSE micrographs. Ti segregates strongly from Cu, with Zr and Cu notably enriched in the regions between the β phase. Glassy regions are identified by selected-area electron diffraction, as illustrated in Fig. 5b. This confirms the co-existence of amorphous phase and crystalline phase, which is the characteristic of metallic-glass-matrix composites (MGMCs).

3.2. Thermal fluid-flow simulations of melt-pool dynamics

Thermal fluid-flow simulations using computational fluid dynamics of VEDs 35 J mm^{-3} and 80 J mm^{-3} were performed to understand dynamics and temperature gradients in the melt pool (Fig. 6). Simulations show two successive laser scans, immediately after one another, on a single powder layer for each VED. Differences in the time instances between the VEDs reflects the differences in scan speed.

As the laser rasters, radiative heating leads to melting of the powder, and a melt pool is formed behind the keyhole. The heating and melting behaviours are similar between the two cases (Fig. 6a and b), but the melt pool for 35 J mm^{-3} is substantially smaller than for 80 J mm^{-3} due to the lower energy input. As shown in Fig. 6c, in the E35 case, the melt-pool edge region between the two tracks is not fully heated (temperature is below 2000 K). In contrast, in the E80 case as shown in Fig. 6d, this edge region is largely heated above the melting temperatures of all pure elements. The simulation suggests that the maximum temperature reached in the melt pool for 35 J mm^{-3} is insufficient to melt all pure elements. For 80 J mm^{-3}, the attained temperature is high enough to melt all elements; if sufficient mixing can occur in the liquid, a homogeneous composition is formed.

If complete mixing can be obtained to produce a uniform liquid, the liquid must be cooled fast enough for the residual Cu-rich liquid to avoid crystallisation and form metallic glass. Cooling rates in L-PBF are typically high, often sufficient to prevent crystallisation upon cooling [51]. Temporal temperature profiles (Fig. 6c–d) suggest that the average cooling rate within the temperature above the glass-transition temperature is 10^6–10^7 K/s for the studied conditions. In comparison to measured critical cooling rates to form binary Cu–Zr glasses [52], this cooling rate is sufficient to form a glass.

The distribution of chemical species for both VEDs is shown after the first laser scan (Fig. 7). Fig. 7a illustrates the distribution of chemical species across the melt pool along the central x-z plane of the scanning laser. The overall composition does not match the nominal composition of the powder layer due to the mixing of the powder with the substrate

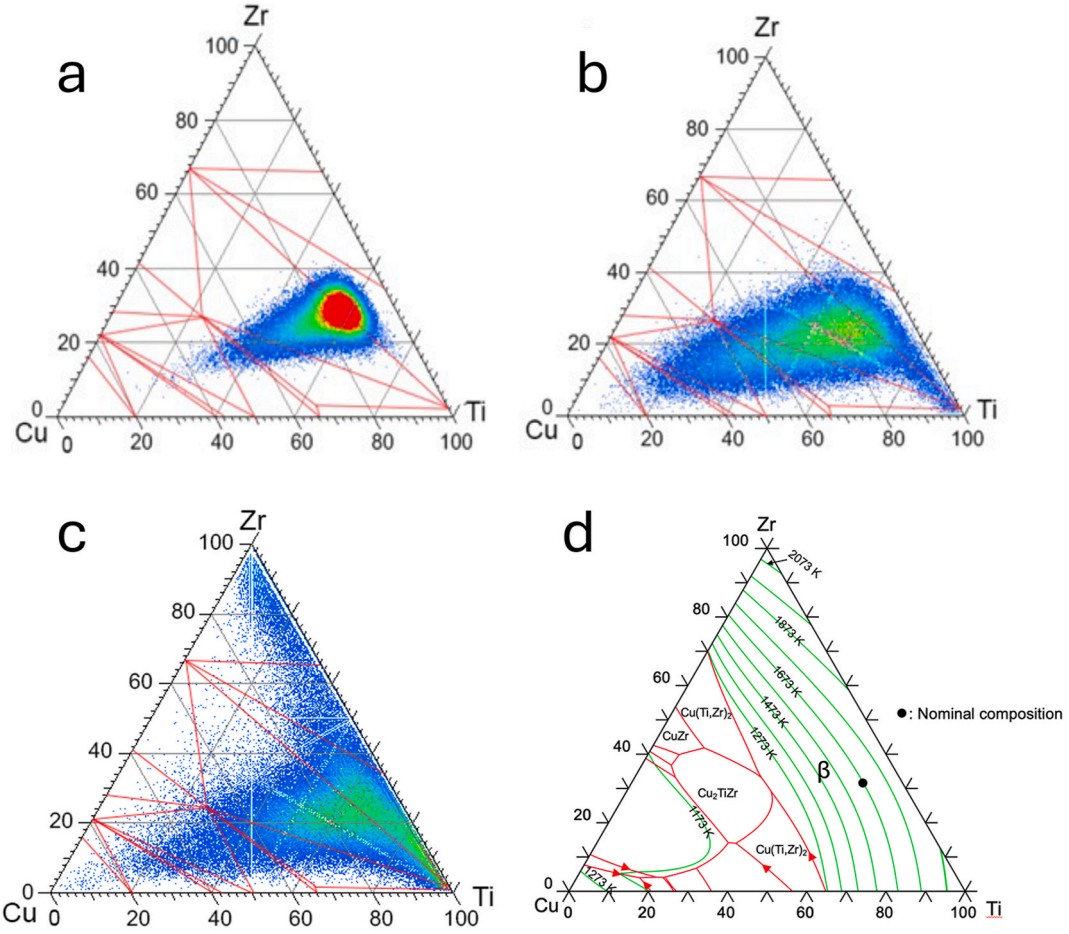

Fig. 4. Ternary chemical heatmaps overlaid with the CALPHAD ternary phase diagram illustrating the compositional variance for (a) E110, (b) E80 and (c) E35. (d) A plot of the liquidus projection of Ti–Zr–Cu shows the variation in the stability of the liquid.

Table 1
Vickers hardness (HV) results for Ti–Zr–Cu specimens processed at different volumetric energy densities (VEDs).

Alloy composition (at.%)	Hardness (HV)	Reference	Marks
Ti-31.5Zr–10Cu	380 ± 22	This work	E110
	404 ± 48	This work	E80
	406 ± 51	This work	E35
Ti-33.25Zr–5Cu	364 ± 6	[29]	
Ti-31.5Zr–10Cu	408 ± 6	[29]	
Ti-29.75Zr–15Cu	437 ± 10	[29]	

material (pure Ti). General trends indicate that mixing becomes more pronounced as the VED increases. It should be noted that while the simulation results reflect the first track and the influence of the initial substrate material (Ti), this trend of enhanced mixing would likely continue with additional layers, even though the quantitative composition may vary.

As shown in Fig. 7b, mixing is more pronounced in the higher-energy-density case of E80, particularly for Ti and Cu species. However, Zr mixing is relatively weaker, which can be attributed to its higher melting temperature and viscosity. In the E35 case, mixing is less developed due to the lower energy input and the reduced melt region, as discussed earlier. The overall trend of enhanced mixing in the higher VED (E80) case is consistent with the experimental EPMA observations shown in Fig. 3, providing a clear explanation for the differences in mixing characteristics under the different laser conditions.

The keyhole region, where heating and turbulence are induced, is expected to behave as a 'stirrer' for the chemical species. The magnitude of the velocity at the depth of the keyhole (110 μm from the surface of the powder layer) is plotted through the progression of the melt pool at eight chosen positions (Fig. 8). For condition $E = 35$ J mm^{-3}, the velocity increases, due to melting and induced Marangoni flow, only once the laser directly heats the region. For $E = 80$ J mm^{-3}, the larger melt pool and slower scan speed means melting and flow occurs before the laser approaches the region, before reaching a higher maximum value once the keyhole arrives due to the higher energy input. Once the laser has passed, convective flow continues for a longer duration for higher VED.

The extent of mixing should correlate with the convective distance L; the cumulative distance travelled by a fluid element:

$$L = \int |\vec{v}| dt. \tag{10}$$

L is calculated from $t = 0$ s to 260 μs. For the condition of 80 J mm^{-3}, a longer convective distance is measured (Fig. 8d) indicative of greater mixing.

4. Discussion

There are numerous economic and academic advantages to avoiding the need for pre-alloyed powders in producing MGs and MGMCs. The present work highlights that to produce MGs and MGMCs in this way, high VED is needed to ensure complete melting and mixing of blended powder. For the present composition, the SEM micrographs and the ternary chemical heatmaps confirm that microstructural heterogeneity and chemical inhomogeneity become more apparent as the energy

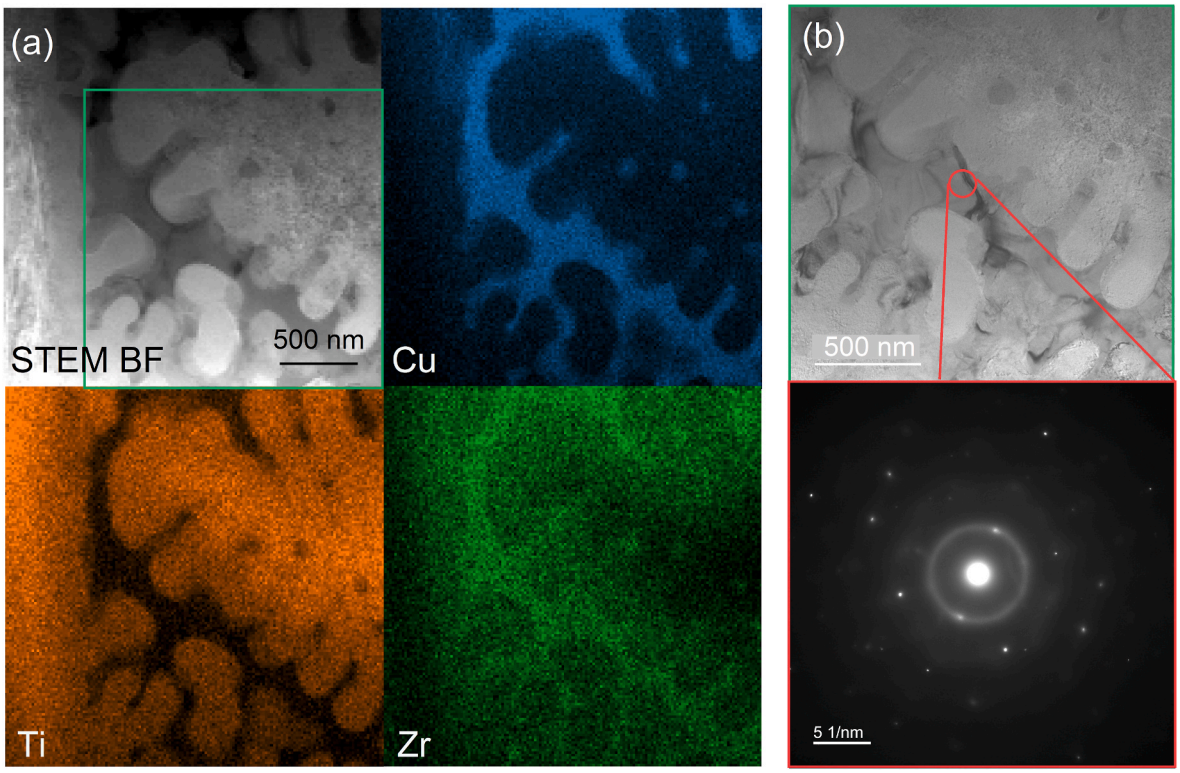

Fig. 5. STEM imaging and analysis of E35 sample within the melt pool. (a) STEM bright-field image of lamellae taken from the melt pool. EDX image reveals Cu- and Zr-rich regions between fingers of unmelted Ti powder. (b) TEM bright-field image of the region highlighted in (a). The diffraction pattern shows amorphous Cu- and Zr-rich regions.

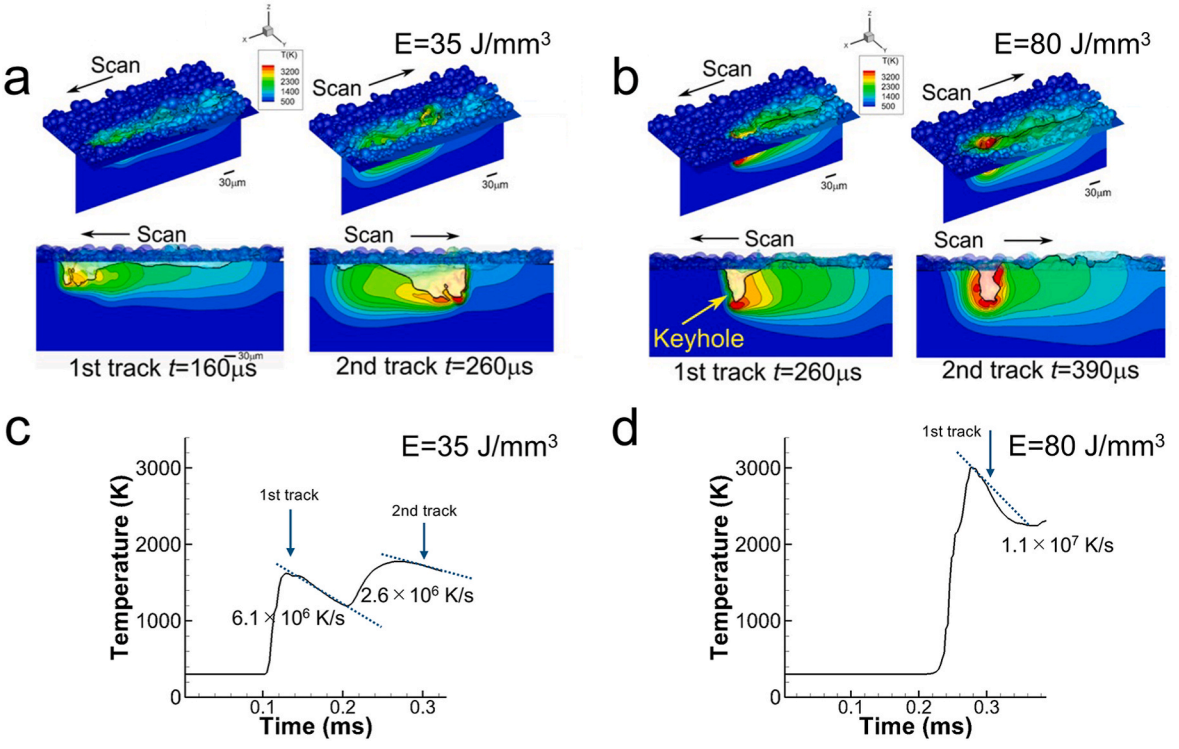

Fig. 6. (a–b) Temperature distribution along the plane of the scanning laser beam centre for E35 and E80, respectively. (c–d) Temperature evolution in the melt-pool edge region between the 1st and 2nd tracks of E35 and E80, respectively. The corresponding cooling-rate calculations are also provided.

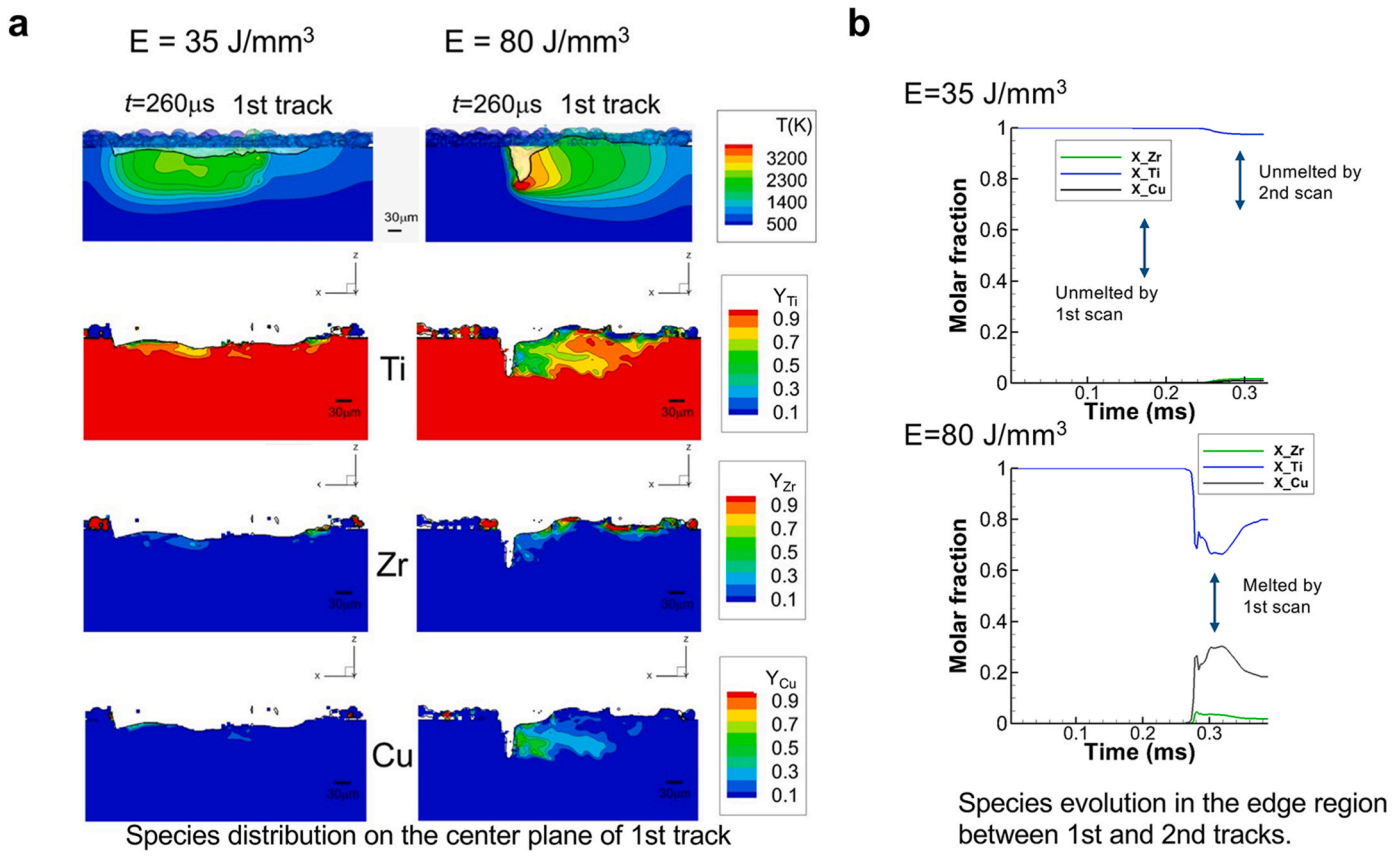

Fig. 7. (a) Temperature field in the melt pool and chemical species distribution after the first track of laser. Y_i is the mass fraction of chemical species *i* (Ti, Zr and Cu) in the range of 0.0–1.0 for each species. (b) Temporal species mixing in the same melt-pool edge region as in Fig. 6c–d.

density decreases.

At a high energy density ($E = 110$ J mm^{-3}), the composition distribution in the 'heatmap' is relatively narrow and primarily centred around the nominal alloy composition. This finding is consistent with XRD analysis and thermodynamic calculations, which identified the formation of primary β-(Ti,Zr) phase and a small fraction of the (Ti, Zr)$_2$Cu phase. As the energy density decreases to $E = 80$ J mm^{-3}, the composition distribution in the 'heatmap' broadens and shifts away from the nominal composition, spreading into areas closer to the eutectic composition predicted by the liquidus projection of the Ti–Zr–Cu system. This observation aligns with SEM/EPMA results, which show that the residual liquid is enriched with Cu and Zr solute atoms. At the lowest energy density of $E = 35$ J mm^{-3}, the composition distribution in the 'heatmap' becomes highly diffuse, agreeing quantitatively with the higher *H* value. In this condition, regions of Ti and Zr enrichment are clearly observed, with some areas having compositions close to pure elemental Ti or Zr. This can be attributed to the presence of unmelted Ti and Zr particles.

To achieve chemical homogeneity, a high VED is essential for complete melting of all elements. However, even when the VED is sufficient for melting, convective flow is necessary to ensure adequate mixing. The impact of insufficient Marangoni convection and limited melt flow on chemical inhomogeneity becomes even more pronounced as the VED decreases. In the melt pool, temperature or composition gradients can generate surface tension differences, leading to Marangoni flow [53–56]. Partial melting and the Marangoni effect are among the key factors affecting composition uniformity during the melting stage of blended powders [57,58]. Increasing the VED amplifies Marangoni forces, promoting better mixing and improving the homogeneity of the melt pool.

Although volumetric energy density (VED) is widely utilised as a key process parameter in additive manufacturing, it does not fully capture the complexities of melt pool behaviour, particularly in blended powder systems. The Marangoni-driven convection, keyhole instability, and thermal fluid interactions introduce additional challenges that significantly influence chemical uniformity and microstructural formation. The interaction between melt pool hydrodynamics, temperature gradients, and local composition variations is especially critical in determining the final material properties.

This influence of energy density on melt-pool behaviour and the resulting microstructural inhomogeneity are summarised in the schematic shown in Fig. 9. At high VED, the slow laser scan speed and extended heating time create a highly dynamic melt pool with intense mixing. The induced Marangoni fluid flow within the melt pool exhibits increased velocity, leading to a longer cumulative travel distance for the liquid elements. This vigorous stirring contributes to enhanced chemical and microstructural homogeneity. In contrast, at low VED, the faster laser scan speed facilitates quicker heat transfer to the outer regions, resulting in a melt pool that becomes slightly shallower and wider. The shorter convective flow distance observed at lower energy densities leads to insufficient stirring for species mixing, resulting in distinct chemical variations and microstructural inhomogeneities. These regions may exhibit species enrichment and may even contain unmelted elemental particles. Enhancing the homogeneity of in-situ alloys can be achieved by increasing the VED, which in turn enhances the Marangoni forces.

For pre-alloyed powders, whose compositions are typically near-eutectic compositions for MGs, the alloy melting point is substantially lower than the pure constituent elements – approximately 20–30% lower than the compositionally weighted-averaged of the melting points of the pure elements [59]. The advantage of these lower melting points on achieving rapid solidification is important to consider. Lower VED

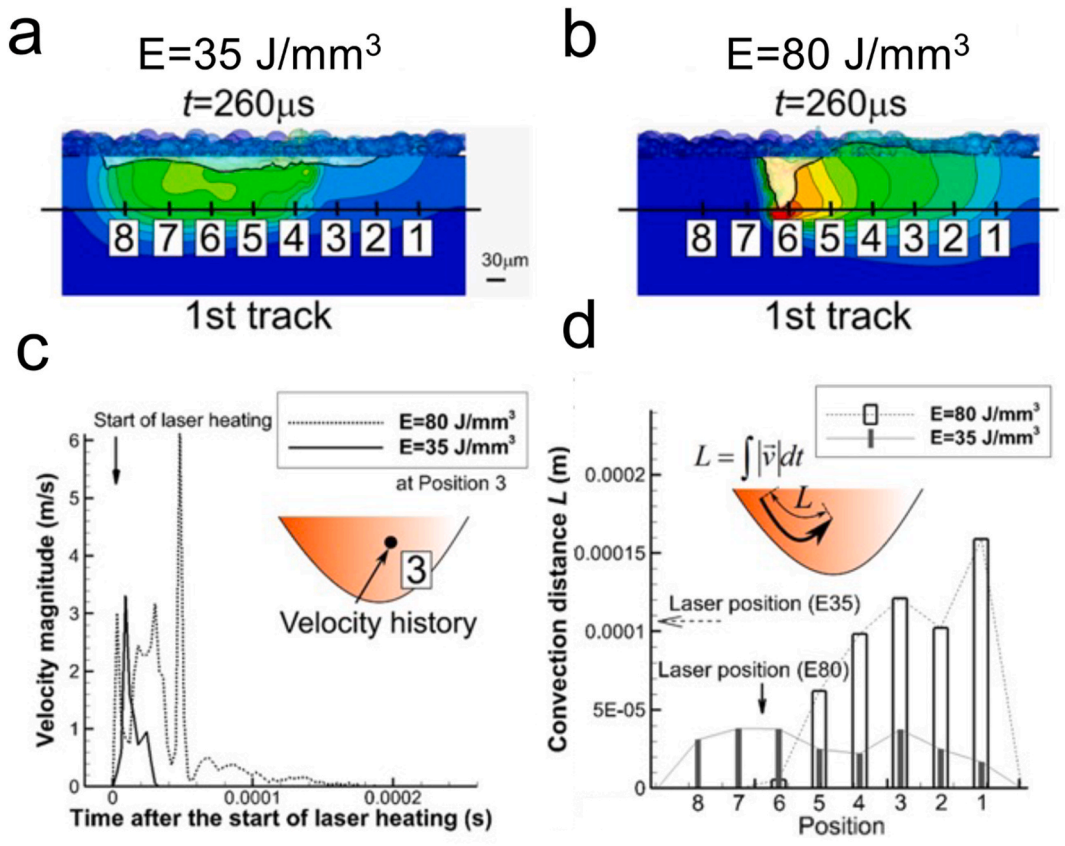

Fig. 8. Velocity magnitude in the melt pool: (a–b) measurement points for the first track of the E35 and E80, respectively. The depth is 110 mm from the powder layer surface. (b) Time history of the velocity magnitude at measurement point 3, and (c) convection distance at each measurement point calculated by the integration of the velocity magnitude. Noted that in the E80 case, the laser position is just ahead of point 6, whereas in the E35 case, the first scan has already been completed, and therefore the laser position is outside the range of this figure.

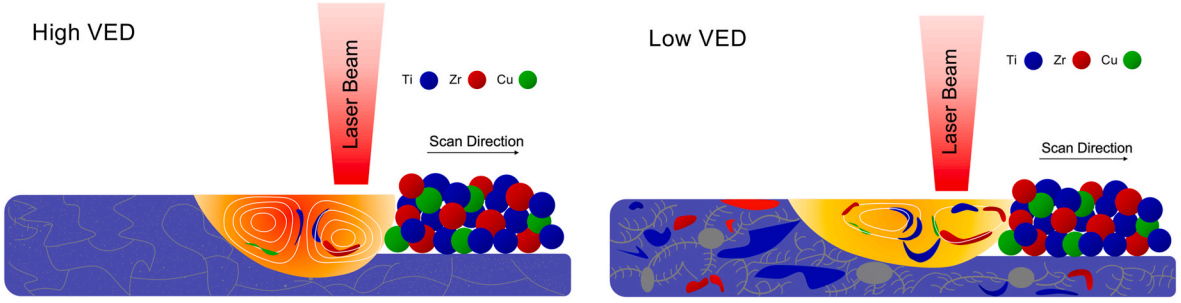

Fig. 9. Schematic illustration of melt-pool dynamics and their impact on microstructural inhomogeneity.

typically leads to higher cooling rates, since the thermal budget for processing is lower [21]. While these increased cooling rates can enhance the amorphous fraction and improve properties such as strength and ductility, they may also hinder the uniform mixing of constituent elements, critical for blended powders. Additionally, a narrow window of processing parameters exists for achieving optimal properties in MGs and MGMCs from blended powders. Precise control over VED, scan speed, and other parameters is necessary; deviations can result in inadequate melting with unmelted particles or excessive cooling rates that negatively impact mechanical properties.

This narrow processing window limits the applicability of this method primarily to MGs and MGMCs that exhibit excellent thermal stability and those that can be processed effectively at lower cooling rates. Materials that do not fall within this category may struggle to achieve the necessary homogeneity and mechanical performance, ultimately restricting the versatility and range of alloys that can be produced using blended powders. Thus, while the use of blended powders offers potential advantages in terms of alloy composition flexibility, the inherent challenges associated with processing conditions necessitate careful consideration of the materials being used and their thermal characteristics.

The observed hardness trends demonstrate the significant influence of volumetric energy density (VED) on microstructure and mechanical properties in Ti–Zr–Cu alloys processed through L-PBF. At higher VED, increased energy input enhances melting and promotes homogeneity, yielding more uniform hardness values. Conversely, at lower VED, phase and compositional segregation leads to increased hardness variation due to the formation of Cu-rich phases and amorphous regions, which exhibit higher hardness than the β-(Ti,Zr) phase. This also effect on the lower hardness due to the existing un-melted particle of the powder in

low VED condition. This trend aligns with previous studies showing that higher Cu content enhances hardness in Ti–Zr–Cu alloys [29]. Similarly, in other alloy systems, higher VED improves mixing efficiency, grain refinement, and mechanical performance [60–62].

Modelling of temperature profiles during each laser scan in the present work are limited in scope. The melt pool for the studied VEDs is substantially larger than a single powder layer. It is computationally too expensive to study in this detail at larger scales. Consideration of temperature profiles in the heat-affected zone is also important. Though the cooling rate may be high enough to initially form a glass, if the temperature in the heat-affected zone rises above T_g, there remains a risk of crystallisation of the glass. Higher VEDs will lead to increase heating in the heat-affected zone. The use of blended elemental powders does not assist in minimising crystallisation in this region.

Our graphical interpretation of (in)homogeneity in the melt pool is not limited in application to AM of MGs and MGMCs. The use of blended powders has garnered interest in many systems where cost-saving is sought or there is limited availability of custom powders [63–68]. In heterostructured materials, the type, quantity and composition of phases can be concisely expressed using ternary or pseudo-ternary mapping of spatially-resolved compositional information. The suggested H factor allows quantification of these charts for effective comparison.

5. Conclusions

This study provides new insights into the processing and microstructural evolution of β-(Ti,Zr)-reinforced metallic-glass-matrix composites (MGMCs) fabricated via laser powder bed fusion (L-PBF) using blended elemental powders. A key novelty lies in integrating experimental characterisation with computational modelling—an approach not fully explored in prior Ti–Zr–Cu studies. This combined methodology offers a predictive framework that extends beyond Ti–Zr–Cu alloys, advancing the field of compositionally complex alloys in additive manufacturing. The main findings are.

- This study bridges experimental characterisation and computational modelling, providing deeper insights into alloy mixing, phase distribution, and microstructural evolution.
- VED governs melt pool behaviour, chemical homogeneity, and microstructural uniformity, significantly impacting mechanical properties.
- Marangoni-driven convection suppresses elemental segregation, ensuring uniform phase distribution.
- Enhanced convective flow promotes complete melting, leading to refined and more homogeneous microstructures.
- The introduced graphical interpretation and quantitative heterogeneity analysis provide a systematic approach for assessing compositional uniformity, applicable to other multi-component alloys.

Declaration of competing interest

The authors declare that they have no known competing financial interests or personal relationships that could have appeared to influence the work reported in this paper.

Acknowledgement

The authors acknowledge the financial support through Transforming Systems through Partnership - Thailand project by Royal Academy of Engineering under Newton Fund programme (TSP2021 \100366). BLW and CPB acknowledge Chulalongkorn Academic Advancement into its 2nd Century Project, (Phase 2), Thailand. OSH and ALG acknowledge the financial support of ERC Project "ExtendGlass". OSH also thanks Goldsmiths' Company Charity, London. CPW would like to acknowledge the funding from UKRI Innovation Fellowship funded by Engineering and Physical Science Research Council (EPSRC), UK Research and Innovation, under the grant number: EP/S000828/2.

References

[1] Schuh CA, Hufnagel TC, Ramamurty U. Mechanical behavior of amorphous alloys. Acta Mater 2007;55(12):4067–109.
[2] Ashby MF, Greer AL. Metallic glasses as structural materials. Scr Mater 2006;54(3):321–6.
[3] Liu G, Zhang X, Chen X, He Y, Cheng L, Huo M, Yin J, Hao F, Chen S, Wang P. Additive manufacturing of structural materials. Mater Sci Eng R Rep 2021;145:100596.
[4] Zhang L, Narayan RL, Fu H, Ramamurty U, Li W, Li Y, Zhang H. Tuning the microstructure and metastability of β-Ti for simultaneous enhancement of strength and ductility of Ti-based bulk metallic glass composites. Acta Mater 2019;168:24–36.
[5] Zuo K, Du P, Yang X, Li K, Xiang T, Zhang L, Xie G. Enhancing the bioactivity and ductility of bulk metallic glass by introducing Fe to construct semi-degradable biomaterial. J Mater Res Technol 2024;28:4162–76.
[6] Aliyu AAA, Panwisawas C, Shinjo J, Puncreobutr C, Reed RC, Poungsiri K, Lohwongwatana B. Laser-based additive manufacturing of bulk metallic glasses: recent advances and future perspectives for biomedical applications. J Mater Res Technol 2023;23.
[7] Duan R, Li S, Cai B, Zhu W, Ren F, Attallah MM. A high strength and low modulus metastable β Ti-12Mo-6Zr-2Fe alloy fabricated by laser powder bed fusion in-situ alloying. Addit Manuf 2021;37:101708.
[8] Huiskes R, Weinans H, Van Rietbergen B. The relationship between stress shielding and bone resorption around total hip stems and the effects of flexible materials. Clin Orthop Relat Res 1992;274:124–34.
[9] Vincent S, Daiwile A, Devi S, Kramer M, Besser M, Murty B, Bhatt J. Bio-corrosion and cytotoxicity studies on novel $Zr_{55}Co_{30}Ti_{15}$ and $Cu_{60}Zr_{20}Ti_{20}$ metallic glasses. Metall. Mater. Trans. A: Phys. Metall. Mater. Sci. 2015;46:2422–30.
[10] Larsson L, Marattukalam JJ, Paschalidou E-M, Hjörvarsson Br, Ferraz N, Persson C. Biocompatibility of a Zr-based metallic glass enabled by additive manufacturing. ACS Appl Bio Mater 2022;5(12):5741–53.
[11] Aliyu AAA, Udomlertpreecha S, Medhisuwakul M, Panwisawas C, Reed R, Puncreobutr C, Khamwannah J, Kuimalee S, Yipyintum C, Lohwongwatana B. A new toxic-free Ti40Zr10Co36Pd14 metallic glass with good biocompatibility and surface behaviour comparable to Ti-6Al-4V. Mater Des 2022;218:110691.
[12] Londoño JJ, Costa MB, Cai F-F, Spieckermann F, Levesque A, Prades-Rödel S, Greer AL, Eckert J, Blatter A. Microalloying as a strategy to modulate antibacterial ion release from metallic glasses. J Alloys Compd 2023;968:172121.
[13] Zhang L, Huang Y, Cheng X, Fan H, Sun Y, Ning Z, Cao F, Sun J. Biocompatibility of a micro-arc oxidized ZrCuAlAg bulk metallic glass. J Mater Res Technol 2021;13:486–97.
[14] Pauly S, Löber L, Petters R, Stoica M, Scudino S, Kühn U, Eckert J. Processing metallic glasses by selective laser melting. Mater Today 2013;16(1–2):37–41.
[15] Sohrabi N, Jhabvala J, Logé RE. Additive manufacturing of bulk metallic glasses—process, challenges and properties: a review. Metals 2021;11(8):1279.
[16] Kube SA, Sohn S, Ojeda-Mota R, Evers T, Polsky W, Liu N, Ryan K, Rinehart S, Sun Y, Schroers J. Compositional dependence of the fragility in metallic glass forming liquids. Nat Commun 2022;13(1):3708.
[17] Hays CC, Kim CP, Johnson WL. Microstructure controlled shear band pattern formation and enhanced plasticity of bulk metallic glasses containing in situ formed ductile phase dendrite dispersions. Phys Rev Lett 2000;84(13):2901.
[18] Zhang L, Pauly S, Tang M, Eckert J, Zhang H. Two-phase quasi-equilibrium in β-type Ti-based bulk metallic glass composites. Sci Rep 2016;6(1):19235.
[19] Alabort E, Tang Y, Barba D, Reed R. Alloys-by-design: a low-modulus titanium alloy for additively manufactured biomedical implants. Acta Mater 2022;229:117749.
[20] Yang Z, Markl M, Körner C. Predictive simulation of bulk metallic glass crystallization during laser powder bed fusion. Addit Manuf 2022;59:103121.
[21] Zhang C, Ouyang D, Pauly S, Liu L. 3D printing of bulk metallic glasses. Mater Sci Eng R Rep 2021;145:100625.
[22] Lashgari H, Ferry M, Li S. Additive manufacturing of bulk metallic glasses: fundamental principle, current/future developments and applications. J Mater Sci Technol 2022;119:131–49.
[23] Frey M, Wegner J, Neuber N, Reiplinger B, Bochtler B, Adam B, Ruschel L, Riegler SS, Jiang H-R, Kleszczynski S. Thermoplastic forming of additively manufactured Zr-based bulk metallic glass: a processing route for surface finishing of complex structures. Mater Des 2021;198:109368.
[24] Cagirici M, Wang P, Ng FL, Nai MLS, Ding J, Wei J. Additive manufacturing of high-entropy alloys by thermophysical calculations and in situ alloying. J Mater Sci Technol 2021;94:53–66.
[25] Liu H, Jiang Y, Yang D, Jiang Q, Yang W. Pores and cracks in the metallic glasses prepared by laser powder bed fusion. J Mater Res Technol 2023;26.
[26] Ouyang D, Xing W, Li N, Li Y, Liu L. Structural evolutions in 3D-printed Fe-based metallic glass fabricated by selective laser melting. Addit Manuf 2018;23:246–52.
[27] Li N, Zhang J, Xing W, Ouyang D, Liu L. 3D printing of Fe-based bulk metallic glass composites with combined high strength and fracture toughness. Mater Des 2018;143:285–96.
[28] Gao X, Lin X, Yu J, Li Y, Hu Y, Fan W, Shi S, Huang W. Selective Laser Melting (SLM) of in-situ beta phase reinforced Ti/Zr-based bulk metallic glass matrix composite. Scripta Mater 2019;171:21–5.
[29] Gao X, Lin X, Yan Q, Wang Z, Yu X, Zhou Y, Hu Y, Huang W. Effect of Cu content on microstructure and mechanical properties of in-situ β phases reinforced Ti/Zr-

based bulk metallic glass matrix composite by selective laser melting (SLM). J Mater Sci Technol 2021;67:174–85.
[30] Yan Q, Yu J, Lin X, Dang M, Shi S, Zhang Y, Huang W. High strength in-situ beta reinforced Ti-based bulk metallic glass composite produced by laser Powder Bed Fusion using elemental powder mixture. Mater Sci Eng, A 2022;833:142559.
[31] Bertoli US, Wolfer AJ, Matthews MJ, Delplanque J-PR, Schoenung JM. On the limitations of volumetric energy density as a design parameter for selective laser melting. Mater Des 2017;113:331–40.
[32] Panwisawas C, Perumal B, Ward RM, Turner N, Turner RP, Brooks JW, Basoalto HC. Keyhole formation and thermal fluid flow-induced porosity during laser fusion welding in titanium alloys: experimental and modelling. Acta Mater 2017;126:251–63.
[33] Qiu C, Panwisawas C, Ward M, Basoalto HC, Brooks JW, Attallah MM. On the role of melt flow into the surface structure and porosity development during selective laser melting. Acta Mater 2015;96:72–9.
[34] DebRoy T, Wei HL, Zuback JS, Mukherjee T, Elmer JW, Milewski JO, Beese AM, Wilson-Heid Ad, De A, Zhang W. Additive manufacturing of metallic components–process, structure and properties. Prog Mater Sci 2018;92:112–224.
[35] Khairallah SA, Anderson AT, Rubenchik A, King WE. Laser powder-bed fusion additive manufacturing: physics of complex melt flow and formation mechanisms of pores, spatter, and denudation zones. Acta Mater 2016;108:36–45.
[36] Trapp J, Rubenchik AM, Guss G, Matthews MJ. In situ absorptivity measurements of metallic powders during laser powder-bed fusion additive manufacturing. Appl Mater Today 2017;9:341–9.
[37] Liu H, Jiang Q, Huo J, Zhang Y, Yang W, Li X. Crystallization in additive manufacturing of metallic glasses: a review. Addit Manuf 2020;36:101568.
[38] Pauly S, Schricker C, Scudino S, Deng L, Kühn U. Processing a glass-forming Zr-based alloy by selective laser melting. Mater Des 2017;135:133–41.
[39] Flint TF, Panwisawas C, Sovani Y, Smith MC, Basoalto H. Prediction of grain structure evolution during rapid solidification of high energy density beam induced re-melting. Mater Des 2018;147:200–10.
[40] Yang L, Ren N, Li J, Panwisawas C, Zhang Y, Xia M, Dong H, Li J. Thermal-solutal convection-induced low-angle grain boundaries in single-crystal nickel-based superalloy solidification. J Mater Sci Technol 2025;208:214–29.
[41] Ali H, Ghadbeigi H, Mumtaz K. Residual stress development in selective laser-melted Ti6Al4V: a parametric thermal modelling approach. Int J Adv Manuf Technol 2018;97:2621–33.
[42] Shinjo J, Panwisawas C. Chemical species mixing during direct energy deposition of bimetallic systems using titanium and dissimilar refractory metals for repair and biomedical applications. Addit Manuf 2022;51:102654.
[43] Roy A, Chhabra R. Prediction of solute diffusion coefficients in liquid metals. Metall. Mater. Trans. A: Phys. Metall. Mater. Sci. 1988;19:273–9.
[44] Gao X, Lin X, Yan Q, Zhang S, Lu J, Zhang T, Feng Z, Tang Y, Huang W. The in-situ β phase reinforced Ti/Zr-based bulk metallic glass matrix composite by selective laser melting. Mater Sci Eng, A 2021;824:141720.
[45] Li X, Roberts M, O'keeffe S, Sercombe T. Selective laser melting of Zr-based bulk metallic glasses: processing, microstructure and mechanical properties. Mater Des 2016;112:217–26.
[46] Luo Y, Xing L, Jiang Y, Li R, Lu C, Zeng R, Luo J, Zhang P, Liu W. Additive manufactured large Zr-based bulk metallic glass composites with desired deformation ability and corrosion resistance. Materials 2020;13(3):597.
[47] Li X, Kang C, Huang H, Sercombe T. The role of a low-energy–density re-scan in fabricating crack-free $Al_{85}Ni_5Y_6Co_2Fe_2$ bulk metallic glass composites via selective laser melting. Mater Des 2014;63:407–11.
[48] Żrodowski Ł, Wróblewski R, Leonowicz M, Morończyk B, Choma T, Ciftci J, Święszkowski W, Dobkowska A, Ura-Bińczyk E, Błyskun P. How to control the crystallization of metallic glasses during laser powder bed fusion? Towards part-specific 3D printing of in situ composites. Addit Manuf 2023;76:103775.
[49] Rocha SSd, Adabo GL, Henriques GEP, Nóbilo MAdA. Vickers hardness of cast commercially pure titanium and Ti-6Al-4V alloy submitted to heat treatments. Braz Dent J 2006;17:126–9.
[50] Qadr HM. Effect of ion irradiation on the hardness properties of Zirconium alloy. Annals of the University of Craiova, Physics 2019;29:68–76.
[51] Yang G, Lin X, Liu F, Hu Q, Ma L, Li J, Huang W. Laser solid forming Zr-based bulk metallic glass. Intermetallics 2012;22:110–5.
[52] Pauly S, Das J, Mattern N, Kim D, Eckert J. Phase formation and thermal stability in Cu–Zr–Ti (Al) metallic glasses. Intermetallics 2009;17(6):453–62.
[53] Chan C, Mazumder J, Chen M. Effect of surface tension gradient driven convection in a laser melt pool: three-dimensional perturbation model. J Appl Phys 1988;64 (11):6166–74.
[54] Rongy L, De Wit A. Steady Marangoni flow traveling with chemical fronts. J Chem Phys 2006;124(16).
[55] Panwisawas C, Perumal B, Ward RM, Turner N, Turner RP, Brooks JW, Basoalto HC. Keyhole formation and thermal fluid flow-induced porosity during laser fusion welding in titanium alloys: experimental and modelling. Acta Mater 2017;126:251–63.
[56] Qiu C, Panwisawas C, Ward M, Basoalto HC, Brooks JW, Attallah MM. On the role of melt flow into the surface structure and porosity development during selective laser melting. Acta Mater 2015;96:72–9.
[57] DebRoy T, Wei H, Zuback J, Mukherjee T, Elmer J, Milewski J, Beese AM, Wilson-Heid AD, De A, Zhang W. Additive manufacturing of metallic components–process, structure and properties. Prog Mater Sci 2018;92:112–224.
[58] Li W, Chen X, Yan L, Zhang J, Zhang X, Liou F. Additive manufacturing of a new Fe-Cr-Ni alloy with gradually changing compositions with elemental powder mixes and thermodynamic calculation. Int J Adv Manuf Technol 2018;95:1013–23.
[59] Li Y, Zhao S, Liu Y, Gong P, Schroers J. How many bulk metallic glasses are there? ACS Comb Sci 2017;19(11):687–93.
[60] Mosallanejad M, Niroumand B, Aversa A, Manfredi D, Saboori A. Laser powder bed fusion in-situ alloying of Ti-5% Cu alloy: process-structure relationships. J Alloys Compd 2021;857:157558.
[61] Han J, Yang J, Yu H, Yin J, Gao M, Wang Z, Zeng X. Microstructure and mechanical property of selective laser melted Ti6Al4V dependence on laser energy density. Rapid Prototyp J 2017;23(2):217–26.
[62] Sohrabi N, Jhabvala J, Kurtuldu G, Stoica M, Parrilli A, Berns S, Polatidis E, Van Petegem S, Hugon S, Neels A. Characterization, mechanical properties and dimensional accuracy of a Zr-based bulk metallic glass manufactured via laser powder-bed fusion. Mater Des 2021;199:109400.
[63] Sing SL, Huang S, Goh GD, Goh GL, Tey CF, Tan JHK, Yeong WY. Emerging metallic systems for additive manufacturing: in-situ alloying and multi-metal processing in laser powder bed fusion. Prog Mater Sci 2021;119:100795.
[64] Wang J, Wang Y, Su Y, Shi J. Evaluation of in-situ alloyed Inconel 625 from elemental powders by laser directed energy deposition. Mater Sci Eng, A 2022;830: 142296.
[65] Simonelli M, Aboulkhair NT, Cohen P, Murray JW, Clare AT, Tuck C, Hague RJ. A comparison of Ti-6Al-4V in-situ alloying in Selective Laser Melting using simply-mixed and satellited powder blend feedstocks. Mater Char 2018;143:118–26.
[66] Mosallanejad MH, Niroumand B, Aversa A, Saboori A. In-situ alloying in laser-based additive manufacturing processes: a critical review. J Alloys Compd 2021; 872:159567.
[67] Zeng J, Yang Y, Peng H, Wang P, Liu C, Chen Z, Chen W, Liu X, Wu Y, Liu Z. Additive manufacturing of high entropy shape memory alloy with outstanding properties through multi-remelting in-situ alloying. Addit Manuf 2024;88:104253.
[68] Shinjo J, Panwisawas C. Digital materials design by thermal-fluid science for multi-metal additive manufacturing. Acta Mater 2021;210:116825.